HSX as an example of a resilient non-resonant divertor ⒡

A. Bader, A. H. Boozer, C. C. Hegna, S. A. Lazerson ⒾⒹ, and J. C. Schmitt

COLLECTIONS

ⒻThis paper was selected as Featured

View Online   Export Citation   CrossMark

ARTICLES YOU MAY BE INTERESTED IN

Key results from the first plasma operation phase and outlook for future performance in Wendelstein 7-X
Physics of Plasmas **24**, 055503 (2017); https://doi.org/10.1063/1.4983629

Performance of Wendelstein 7-X stellarator plasmas during the first divertor operation phase
Physics of Plasmas **26**, 082504 (2019); https://doi.org/10.1063/1.5098761

Core radial electric field and transport in Wendelstein 7-X plasmas
Physics of Plasmas **25**, 022508 (2018); https://doi.org/10.1063/1.4999842

HSX as an example of a resilient non-resonant divertor

A. Bader,[1] A. H. Boozer,[2] C. C. Hegna,[1] S. A. Lazerson,[3] and J. C. Schmitt[4]
[1]*University of Wisconsin-Madison, Madison, Wisconsin 53706, USA*
[2]*Columbia University, New York, New York 10027, USA*
[3]*Princeton Plasma Physics Laboratory, Princeton, New Jersey 08540, USA*
[4]*Auburn University, Auburn, Alabama 36849, USA*

This paper describes an initial description of the resilient divertor properties of quasi-symmetric (QS) stellarators using the HSX (Helically Symmetric eXperiment) configuration as a test-case. Divertors in high-performance QS stellarators will need to be resilient to changes in plasma configuration that arise due to evolution of plasma pressure profiles and bootstrap currents for divertor design. Resiliency is tested by examining the changes in strike point patterns from the field line following, which arise due to configurational changes. A low strike point variation with high configuration changes corresponds to high resiliency. The HSX edge displays resilient properties with configuration changes arising from the (1) wall position, (2) plasma current, and (3) external coils. The resilient behavior is lost if large edge islands intersect the wall structure. The resilient edge properties are corroborated by heat flux calculations from the fully 3-D plasma simulations using EMC3-EIRENE. Additionally, the strike point patterns are found to correspond to high curvature regions of magnetic flux surfaces. *Published by AIP Publishing.*
[http://dx.doi.org/10.1063/1.4978494]

I. INTRODUCTION

The "divertor" problem is a major issue for next generation stellarators.[1–5] A proper divertor needs to (1) limit heat loads on the first wall to acceptable levels,[6–9] (2) allow sufficient neutral pressure for pumping,[10–13] and (3) prevent the influx of impurities into the main plasma.[14–17] The basic idea of a divertor concept in any confinement scheme is to move the region where the hot plasma interacts with the solid vessel away from the last closed flux surface.[18] In tokamaks, this is most commonly achieved by creating one or two nulls in the poloidal field, which define a separatrix. The confined plasma that crosses the separatrix is swept to target plates, which can be positioned a distance from the main confined plasma.

In stellarators, the divertor problem is not solved, and there are a variety of concepts under consideration. This paper focuses on the outlook for divertors for quasi-symmetric (QS) stellarators. While QS stellarators possess desirable properties for core plasmas,[19–21] they are not able to take advantage of the divertor designs used in devices with helical coils (such as LHD, the Large Helical Device[22]) or in configurations that optimize for low bootstrap current (such as Wendelstein 7-X[23,24]).

To examine divertor behavior in QS stellarators, we introduce the concept of resilient divertors.[25] A resilient divertor is a divertor configuration that is robust to changes that arise from the plasma evolution. As a plasma evolves from start-up to its steady state operating point, the magnetic configuration can alter as bootstrap currents and plasma pressure evolve and increase. These can affect both the core and edge behaviors. In this paper, we will examine the alteration of divertor behavior in stellarators as the configuration is changed. The goal is to find characteristics of the edge that make the divertor structure resilient to changes in the plasma shape, the plasma pressure, and even the magnetic topology. If the plasma surface interaction region is robust to evolving plasma conditions, divertor armor, baffles, and other structures can be more easily designed. The key element is that we seek divertor configurations that are not dependent on a resonance at the edge that is susceptible to large island formation. The appearance of magnetic islands that intersect target surfaces can eliminate the resilient divertor feature. Therefore, low order resonances, n/m, where n is a multiple of the field periods, should be avoided.

In this paper, we explore some properties of non-resonant divertors using the magnetic geometry of Helically Symmetric eXperiment (HSX) as a test case. HSX is optimized for quasi-symmetry[26] and therefore can serve as a test-bed for QS stellarators.

The layout of the paper is as follows: Before introducing the details of the HSX geometry, it is first necessary to provide some broad introduction to stellarator divertors and to explain how they differ from their simpler tokamak cousins. Thus, Section II discusses some background to stellarator edge geometries. In Section III, we discuss two methodologies for calculating the strike lines, which will be used for the test of resilience. In Section IV, we describe various ways to vary the configuration. Section V gives the results of the calculations and shows that strike point patterns are robust as long as wall elements do not intersect large edge islands. Section VI discusses a basic metric to evaluate whether a configuration is resilient or not. Section VII verifies the simple strike point model in specific cases with the full wall heat flux calculation from EMC3-EIRENE. Finally, Section VIII discusses the results and provides some geometrical properties for the behavior of various magnetic configurations.

II. STELLARATOR EDGE GEOMETRIES

Before addressing the stellarator edge, first we consider the simpler two dimensional edge of a diverted tokamak. In a tokamak, there exists one or more poloidal nulls where the magnetic field in the poloidal direction goes to zero. We consider first the simplest case of an ideal single poloidal null. The location of this null defines the last closed flux surface (LCFS), with normalized flux surface label $r = a$. All field lines with normalized $r < a$ are confined, and all field lines with $r > a$ are unconfined. Field lines that asymptotically approach the poloidal null are on the separatrix that divides the confined and unconfined regions. Any field line in the unconfined region will strike a target plate, and the characteristic distance for a field line from target to target, referred to here as $2L_c$, is the pitch of the magnetic field times the circumferance, or $2\pi R q$ or, in terms of the rotational transform, ι, $2\pi R/\iota$. For a tokamak with multiple null points, the characteristic length is given by $2\pi R/N\iota$, where N is the number of null points.

As a first departure from tokamak geometry, we examine the edge of a torsotron or a heliotron, such as LHD, where the field line pitch is generated by a set of external helical coils. There is also a null that determines a separatrix in this geometry as well, but the null rotates helically. In an idealized periodic cylindrical limit, for each helical coil, there is a corresponding null. The helical pitch of the external coils causes the nulls to rotate around the edge. Nevertheless, the connection length for points outside the separatrix is still given $2\pi R/N\iota$. As helical symmetry cannot be enforced in a toroidal configuration, this idealized picture is only an approximation given a set of helical coils. The presence of 3D fields and field line resonances complicates this simple description.

In stellarators with modular coils, it is not possible to create an axisymmetric divertor like the poloidal divertor in tokamaks. Also, with the absence of helical coils, a helically continuous divertor, like the helical divertor in LHDs, may not be available. One solution is to use an "island divertor."[24] In this geometry, there are multiple nulls, the number of which is determined by the periodicity of the machine and the value of ι. Wendelstein 7-X (W7-X) is a five period machine that typically operates with edge near $\iota = 1$. Thus, the dominant resonant mode has $n = 5$, $m = 5$. There are five nulls. The major difference between the island divertor and the helical divertor is not the number of nulls but rather that the connection length to the target is governed by the field line pitch of the island separatrix. This island pitch is given by $r_i \iota'$, where r_i is the width of the island and ι' is the shear in the iota profile.[27] Thus, the characteristic connection length in an island divertor is $2\pi R/Nr_i\iota'$. One immediate consequence of this difference is that optimized stellarators are usually designed to have low shear to avoid magnetic resonances;[28] therefore, the connection length can be many times longer in stellarators with island divertors than in tokamaks.[29] Due to these differences, a number of properties of stellarator divertors differ from tokamaks.[27]

The island divertor has met with success in W7-AS[30] and is the basis for the W7-X design, where the $\iota = 1$ resonance surface produces a 5/5 island. The main difficulty with the island divertor is that the position of the edge island chain is highly sensitive to the rotational transform profile, which can change with plasma pressure and bootstrap current.[31] The Helias line of stellarators is specifically designed to reduce the bootstrap currents so that the position of the edge island can be carefully controlled. The island divertor idea is only suitable for stellarators with limited bootstrap currents. It is considerably more difficult to design an island divertor for a quasi-symmetric stellarator where substantial bootstrap currents are expected as plasma pressure rises. Such a device would require accurate models of pressure and bootstrap currents in order to determine an operating point at which the divertor structures are designed. Furthermore, an island divertor for a QS stellarator would require accurate control of the plasma current using either current drive or external coils in the start-up phase. A non-resonant divertor simplifies these requirements greatly.

In reality, in addition to the null points induced by the helical coils in the helical divertor and the low order resonance of the island divertor, there are many other resonances present. In these geometries, the main effect of the resonances is to cause island overlap induced magnetic stochasticity between the good flux surfaces of the confined plasma and the well-defined field lines internal to the magnetic island or in the divertor legs.[32,33] That is to say, there is a stochastic layer between the confined plasma and the unconfined plasma. A consequence of this stochastic layer is that the separatrix is not well defined. Connection lengths approach infinity as you near the confined plasma and approach the ideal limit, L_c, as you approach the unconfined region. This behavior can also be induced in tokamaks with the presence of magnetic perturbations.[34]

At this point, it is possible to discuss the edge geometry of the non-resonant divertor. In Boozer's description of non-resonant divertors,[25] the dominant feature for these geometries is the presence of sharp ridges in flux surfaces near the LCFS. These can be visualized as regions of high curvature of the flux surface shape. Poloidally local to these ridges, field lines are forced to follow along them, meaning that the direction of the peak curvature is perpendicular to the field line. This is reminiscent of an X-point on the tokamak divertor, although it rotates helically, and it only exists for a fixed toroidal extent of the surface where the ridges are sharp. In this case, the edge is dominated by the presence of higher order resonances. However, magnetic islands that do exist tend to be not well formed.

The calculation of the principal curvature of the surface is made in the following manner. First, the surface is parametrized into two coordinates. In the following, we use a poloidal-like direction, u, and a toroidal-like direction, v. Let X, Y, and Z be points on the surface in Cartesian coordinates. Define the vector $\mathbf{r}_u = X_u\mathbf{i} + Y_u\mathbf{j} + Z_u\mathbf{j}$, where X_u, Y_u, and Z_u are the partial derivatives in the poloidal direction. Similarly, define $\mathbf{r}_v$ and the second derivative vectors $\mathbf{r}_{uu}$, $\mathbf{r}_{uv}$, and $\mathbf{r}_{vv}$. Then, the coefficients of the first fundamental form are given by

$$E = \mathbf{r}_u \cdot \mathbf{r}_u, \tag{1}$$

$$F = \mathbf{r}_u \cdot \mathbf{r}_v, \qquad (2)$$

$$G = \mathbf{r}_v \cdot \mathbf{r}_v. \qquad (3)$$

Next, we define a unit normal to the surface

$$\mathbf{n} = (\mathbf{r}_u \times \mathbf{r}_v)/|\mathbf{r}_u \times \mathbf{r}_v|. \qquad (4)$$

Then, the coefficients of the second fundamental form are given by

$$L = \mathbf{r}_{uu} \cdot \mathbf{n}, \qquad (5)$$

$$M = \mathbf{r}_{uv} \cdot \mathbf{n}, \qquad (6)$$

$$N = \mathbf{r}_{vv} \cdot \mathbf{n}. \qquad (7)$$

The mean curvature is given by

$$K_m = (EN + GL - 2FM)/2(EG - F^2). \qquad (8)$$

The Gaussian curvature is

$$K_G = (LN - M^2)/(EG - F^2). \qquad (9)$$

Finally, the two principal curvatures are given by

$$K_{p1} = K_m + (K_m^2 + K_g)^{1/2}, \qquad (10)$$

$$K_{p2} = K_m - (K_m^2 - K_g)^{1/2}. \qquad (11)$$

The first principal curvature represents the maximum curvature at a given point. In order to provide a simple normalization, in all plots in this paper, the principal curvature is multiplied by the local minor radius.

A. HSX as a non-resonant divertor

As a case study, we use the HSX geometry as an example of a divertor that in its normal operation does not rely on large islands at the magnetic boundary. HSX is a four field period configuration and is therefore susceptible to island formation when the toroidal mode numbers are integer multiples of four. While an $n = 8$, $m = 7$ magnetic island does exist just outside the LCFS of this configuration the edge does exhibit some features similar to those of resonant island divertors,[35,36] the islands do not have internal well-formed helical flux surfaces and, as we will see, the dominant heat flux pattern is resilient to moderate changes in the edge topology.

A 3-D image of the LCFS of HSX is shown in Figure 1. Also, plotted are a few field lines that follow along the sharp ridges. However, because the ridges do not close on themselves, the field lines will eventually leave the regions of the peak curvature. This can be more clearly seen in Figure 2. Here, we show the principal curvature of the LCFS for one field period. In addition, two field lines are followed from the points of the peak curvature. The field lines follow the region of high curvature until the value drops below approximately 50% of the peak.

III. STRIKE POINT CALCULATION METHODOLOGY

As a means of evaluating the edge properties of a given magnetic configuration, we focus mainly on strike-point
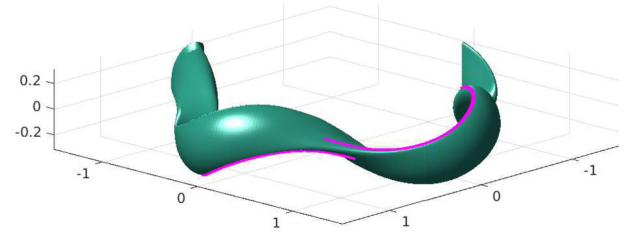

FIG. 1. 3 quarters of the LCFS for the HSX standard configuration with two field lines overplotted in magenta. The field lines follow the ridges for some finite extent.

calculations. In these calculations, magnetic field lines are followed from inside the plasma out to the edge and the locations at where they intersect the wall are recorded. These calculations have the advantage of being relatively fast compared to more detailed heat and particle flux calculations from 3-D simulations like EMC3-EIRENE.

The field line following is done by first starting with a random assortment of points inside the LCFS. The points are followed along the field line by solving the equation $d\boldsymbol{l} \times \boldsymbol{B} = 0$. In cylindrical coordinates, this is given by

$$dr/d\zeta = rB_r/B_\zeta, \qquad (12)$$

$$dz/d\zeta = rB_z/B_\zeta, \qquad (13)$$

where r, z, ζ represent the coordinates in cylindrical geometry, and B_r, B_z, B_ζ are the components of the magnetic field in the respective directions, i.e., $B_r = \mathbf{B} \cdot \nabla r$.

Of course, field lines that start inside the plasma will never intersect a wall outside the plasma. Therefore, in this paper, we use two different methods to move or "diffuse" the field lines outward. The first method is as follows: After each explicit step, a random displacement is supplied to the trajectory in a direction perpendicular to the magnetic field. Thus, the magnetic field lines diffuse, and the motion is that of a particle with diffusion but without any drifts or bounces. This method has been used in many previous calculations (see, for example, Ref. 37) and in general appears to be a good approximation for calculating locations of the peak
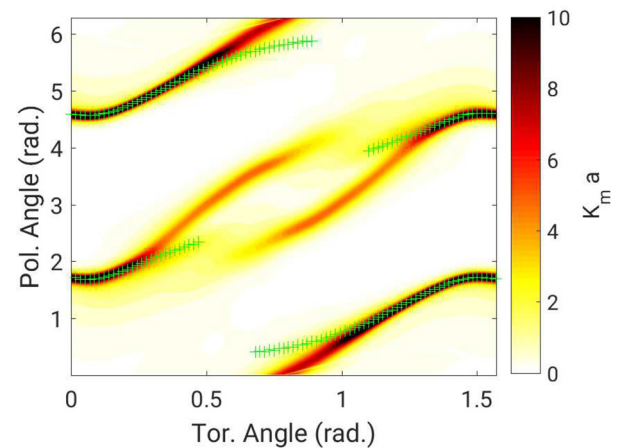

FIG. 2. Contour plot of the principal curvature of the LCFS for one field period normalized to the local minor radius. Overplotted in magenta pluses are the trajectories of two field lines on the surface.

particle and heat flux. In this paper, we will call this method the "diffusion" method.

In addition, it is interesting to determine the location of the field line strike points in the limit as the magnetic diffusion goes to zero. In practice, this is difficult to calculate, even with the efficient field line following algorithms. However, the calculation becomes tractable if instead of diffusing in a random perpendicular direction, the field lines always diffuse outward radially. In this manner, the field lines "spiral" out from inside the plasma, through the separatrix and into the unconfined region.[38] Provided that the coefficient for diffusion is small enough, the calculation yields the strike point location for the first escaping flux tube. We will call this second method the "spiraling" method. In the limit of very small diffusion coefficients, both methods approach the same answer (see Figure 5 and discussion in Section V).

For a proper calculation, it is imperative that starting points lie inside the confined region. This is necessary because the flux through the last closed surface is not necessarily uniform. However, in the confined region, constant density on any flux surface is a reasonable assumption. If points were begun in the unconfined region, as was common in early calculations,[37] the starting point locations may be locations where no actual plasma will ever reach.

IV. CONFIGURATION VARIATIONS

There are three different methods of varying configurations. The first method of varying configuration involves changing the spacing between the last closed flux surface and the target plates. For the basic analysis presented in this paper, we generate a vessel by stepping out from a last closed flux surface. The last closed flux surface is generated from VMEC[40] in a free boundary mode with no internal currents, no plasma pressure, and only contributions from the main set of coils. Then, a vessel is formed by generating a new surface with uniform distance from that last closed flux surface. The leftmost plot of Figure 3 shows the results for various wall positions along with Poincaré plots for flux

surfaces in the standard HSX configuration. Calculating strike points as a function of wall positions is fast to compute, as it does not require making a magnetic grid and only varying the termination condition for the field line following.

The second method of varying configurations includes internal plasma currents directly. In order to include the internal currents, we again use VMEC in a free boundary mode to generate an equilibrium that includes finite plasma current and pressure. The choice of current and pressure profiles used for the simulation are described in Section V C. After a VMEC equilibrium is obtained, a magnetic grid is generated using the FIELDLINES module.[39] For the extrapolation outside the LCFS, the method is similar to that described in the appendix of Ref. 41.

One limitation of VMEC is that magnetic islands are not properly represented inside the core plasma; therefore, we are limited to examining equilibria that do not contain low order resonances at or near the edge. For these calculations, we avoid current values where the $\iota = 1$ resonance is near the edge.

The third method is to use additional external coils to modify the plasma profiles. Specifically, these can be used to alter the iota profile and thus change the structure of the plasma edge. This method has the advantage in that some of the variations are available for experimental testing. Poincaré plots for two configurations made by altering external coils are shown in the right two plots of Figure 3. The disadvantage is that the ultimate goal is to test for configurations with an internal plasma current profile. Internal currents can only be approximated with external coils.[42]

V. ANALYSIS OF STRIKE POINT CALCULATIONS

A. Comparison of field line following methodologies

As a first result, we compare the calculation for the diffusion and spiraling methodologies. The strike point positions on the wall are converted into poloidal angle via a length-normalized mapping. Because the machine is periodic with $N = 4$, the toroidal angle is taken modulo $\pi/2$. All plots in this paper will show only one period in the toroidal direction. The field lines are followed forwards and backwards and are plotted for both methods in Figure 4. For the diffusion calculation, $D = 0.5$ m^2/s, and the calculation assumes an 80 eV proton. For the spiral method, the calculation takes outward steps of 20 μm every 20°. The most salient results are the following. For the magnetic diffusion case, the field lines lie on helical lines, usually two separate strike locations for any toroidal angle. For the spiraling method, the strike points lie in discrete locations in both toroidal and poloidal space. We note that the results are nearly exactly symmetric for both simulations. The symmetry is a result of following in both directions. It is somewhat easy to verify that the strike locations for the spiraling method in the forward direction are the mirror image of the strike locations for the reverse direction. This is true for the diffusion method as well. Because of the symmetry, for most of the rest of the calculations in this paper, we only follow in one direction, with the knowledge that the reverse direction will be the mirror image.
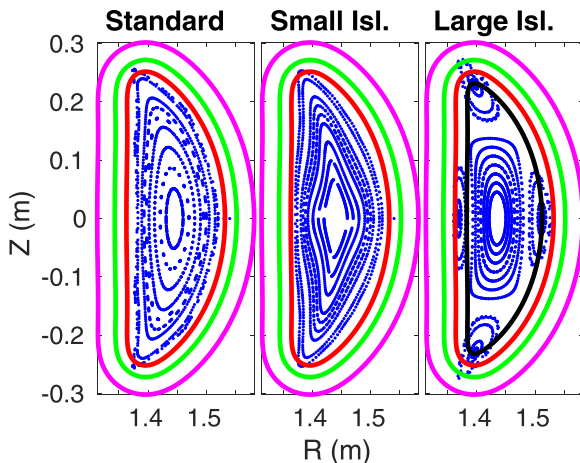

FIG. 3. Poincaré plot with the wall position for small island configuration. Poincaré plots are in blue. Wall positions are 7 cm outside LCFS (magenta), 4 cm (green), 2 cm (red), and 0 cm (black).
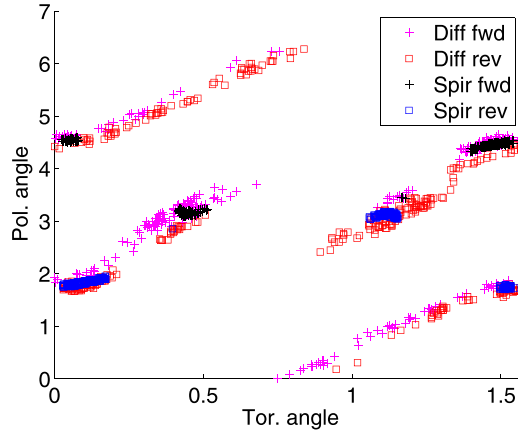
FIG. 4. Strike point scatter plot for magnetic diffusion (red/magenta) and spiral (blue/black) for forward (pluses) and reverse (squares) directions.

In Figure 5, the strike point patterns are plotted for different values of the diffusion coefficient. As the diffusion value is lowered, the strike points become toroidally distinct and approach the results from the spiraling method.

B. Comparison of different wall positions

As a first test of the resiliency of the HSX configuration, the wall is placed at different positions from the LCFS. Results are shown in Figures 6 and 7 where it is seen that using either the diffusion or the spiraling method, the position of the helical strike lines does not differ significantly between the 4 cm and 7 cm positioning. At the 2 cm positioning, the strike lines do differ a little bit. It is possible to see a splitting of the strike lines in both the diffusion and the spiraling method, but it is more clearly delineated in the spiraling method (Figure 7). Nonetheless, it is clear from these calculations that the strike point patterns are robust with respect to the wall location.

C. Including plasma current

Next, we examine equilibria with finite plasma current. To calculate configurations with finite plasma current, we first calculate an equilibrium with VMEC and then generate
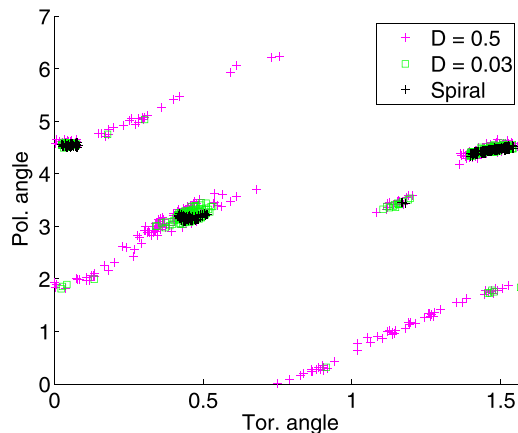

FIG. 5. Strike point scatter plot for magnetic diffusion, $D = 0.5$ m^2/s (magenta), $D = 0.03$ m^2/s (green), and spiral (black).
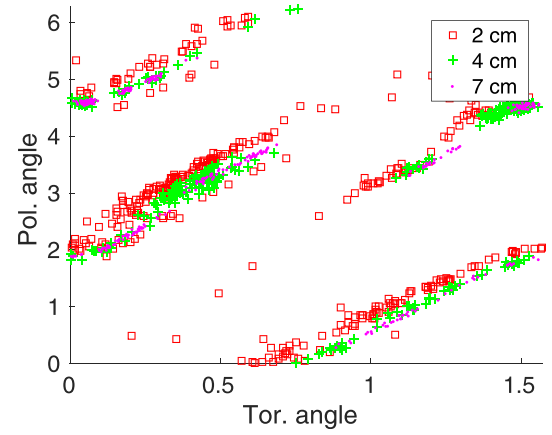

FIG. 6. Strike point scatter plot for magnetic diffusion at three different wall positions 2 cm outside LCFS (black squares), 4 cm (blue +), and 7 cm (red dot).
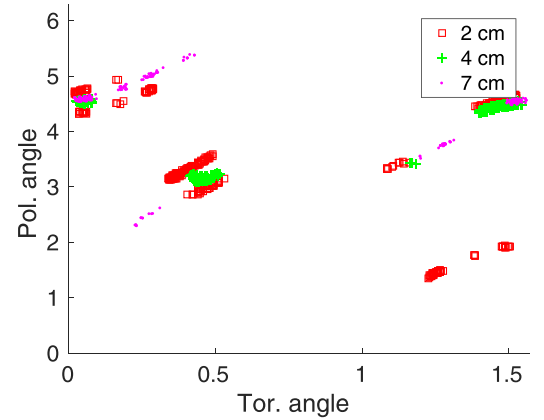

FIG. 7. Strike point scatter plot for spiraling out at three different wall positions, 2 cm outside LCFS (black squares), 4 cm (blue+), and 7 cm (red dot).

a magnetic grid with the FIELDLINES module.[39] To calculate the equilibria, we must choose current and pressure profiles. For the choice of the plasma current profile that crudely approximates a bootstrap current, we assume that $\mathbf{J} \cdot \mathbf{B}$ is zero at the magnetic axis and at the edge. A parabolic representation of $\mathbf{J} \cdot \mathbf{B}$, as shown in Figure 8, is a simple approximation that satisfies these constraints. Three equilibria are examined: a zero current case that corresponds to the
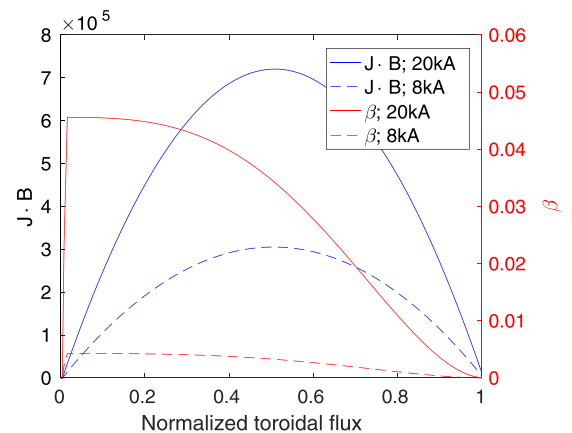

FIG. 8. Current and plasma pressure profiles for the 8 kA and 20 kA configurations from VMEC.
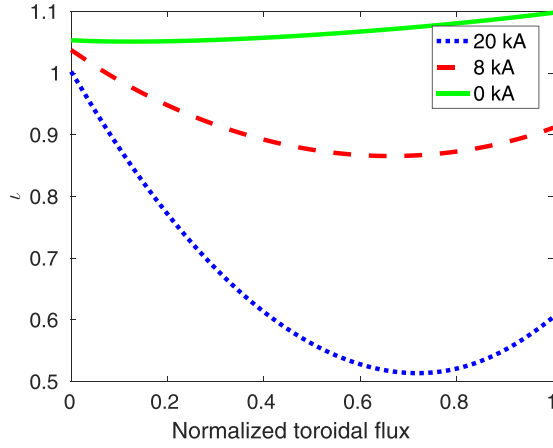
FIG. 9. Rotational transform (ι) profiles for the 0 kA, 8 kA, and 20 kA configurations from VMEC.

FIG. 11. Comparisons of strike points for 0 kA (green dot), 8 kA (red o), and 20 kA (blue +).

standard configuration from Section IV, a medium current case, and a high current case. The current and pressure profile inputs are provided in Figure 8. In the standard case, $\iota > 1$ throughout the entire plasma volume (Figure 9). In the cases with current, ι passes through the $\iota = 1$ surface near the plasma core and is below one in the majority of the plasma. Most importantly, the $\iota = 1$ surface is far from the edge in all cases.

In addition to altering the ι profile, the inclusion of plasma current also has a significant effect on the shape of the LCFS. The plasma current tends to unwind the vacuum transform that causes the sharp edges of the flux surfaces to be smoother and hence reduces the peak curvature. Flux surfaces for $\zeta = 0°, 22.5°,$ and $45°$ are shown in Figure 10.

To move from the VMEC equilibrium to the magnetic field, we use the FIELDLINES module.[39] This code provides a magnetic grid based on the equilibrium, which can then be used for the field line integration in the same manner as the vacuum fields examined in Section V B. The results for the field line strike points for the zero, medium, and high current configurations are shown in Figure 11. There is little difference in the strike point patterns when plasma current is introduced. The conclusion is that for these configurations, the
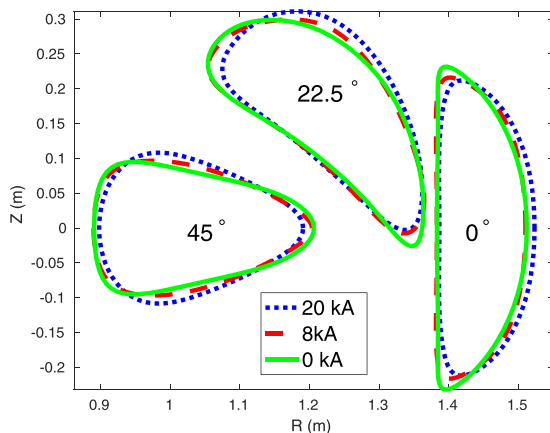
strike point locations are robust to changes in the shape of the core plasma caused by additional plasma current and pressure. The implication is that a single physical structure should be usable as a QS stellarator transitions from startup to high-pressure/bootstrap current operation.

D. Changing configurations with external coils

We now turn to configuration changes with the auxiliary coils. The HSX experiment is equipped with auxiliary coils that can be used to add or the subtract toroidal field. For core transport, these coils can be used to weaken quasi-symmetry;[43] however, they can also be used to modify edge configurations by modifying the rotational transform profile. Using Biot-Savart field line calculations with the external coils allows for an examination of the role of edge islands on the strike point calculation.

In the standard HSX configuration, the rotational transform at the edge is 8/7, which gives the dominant magnetic island chain of $n = 8$, $m = 7$. We term this the medium island configuration. By lowering the rotational transform profile with the external coils, the 8/7 islands can be moved further out towards the wall. At some point, the largest island in the edge is $n = 16$, $m = 15$. Since this dominant island chain is small and the edge fields are stochastisized somewhat, we call this the small island configuration. At higher currents in the auxiliary coils, the $\iota = 1$ surface can be moved towards the edge creating very large $m = 4$, $n = 4$ islands and hence the large island configuration. Poincaré plots for all three configurations are shown in Figure 3. These three configurations were examined in detail in Ref. 36 where it was found that the large island configuration possessed fundamentally different edge behavior with regard to transitions to high recycling and detached regimes.

For the small island configuration, the wall is moved to three positions at varying distances from the LCFS. These positions were included on the Poincaré plot in Figure 3. In order to keep the comparison simple, the shape of the wall is derived from the medium island configuration. Therefore, it is identical to the wall positions examined in Section V B.

FIG. 10. Comparisons of flux surfaces for 0 kA, 8 kA, and 20 kA shown for toroidal angles, $0°$, $22.5°$, and $45°$.

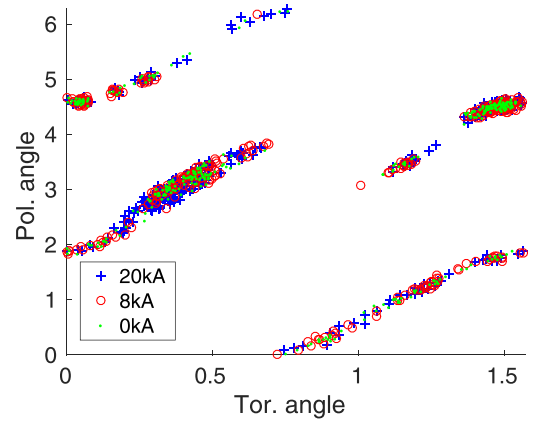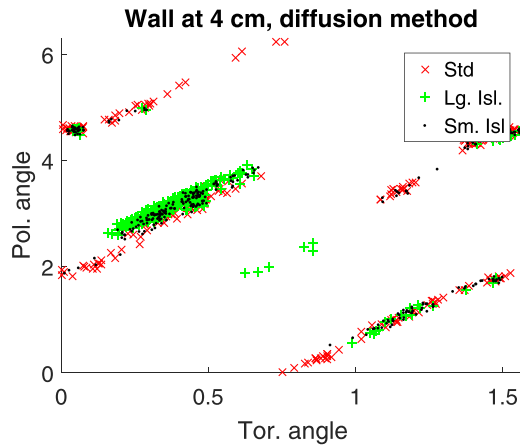FIG. 12. Strike point scatter plot for three configurations with the wall at 4 cm outside LCFS. The configurations are standard (red x), large island (green +), and small island (black dot).

With the auxiliary coils, it is also possible to introduce a resonant or an island divertor. This is possible for the large island configuration shown in Figure 3.

The strike lines for the three configurations with wall positions at 4 cm and 2 cm are given in Figures 12 and 13. At 4 cm, the wall is mostly outside the island extent, and the three configurations have roughly the same strike pattern, although there are a few large island points that do fall in areas not covered by the standard configuration. At 2 cm, there are significant differences in the strike point location, particularly in the large island case. There are two regions where many points impact that do not appear in the standard island configuration. These two regions have been circled in Figure 13 for convenience. The result indicates that the HSX standard configuration is not resilient to variations that introduce large islands that intersect the wall.

We attempt to verify that it is actually the islands that are causing a difference in the strike point calculation rather than a shift of the magnetic axis, by eliminating the effect of the axis shift. This is done by shifting the vessel the same direction and distance as the shift of the magnetic axis. An example of the shifted vessel for the large island configuration is shown
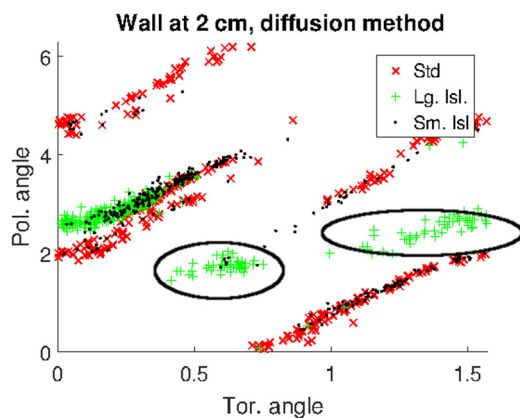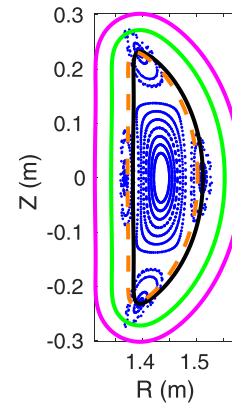

FIG. 14. Poincaré plot for the large island configuration showing vessel positions at 4 cm (green), 0 cm (black), and 0 cm but with a shift to compensate for the magnetic axis (orange-dashed).

in Figure 14. With the shifted vessel, the strike points still fall on different areas (Figure 15), indicating that there is a substantial effect from the island on the edge field line topology. It is clear that if a magnetic topology has large islands in the edge, then the divertor structures will need to be designed to handle it. More importantly, the results imply that it may be very difficult to design a divertor that can operate well for designs that have edge topologies with and without large edge magnetic islands in the standard operational regimes.

VI. EVALUATING RESILIENCE

In this section, we attempt to provide some evaluation on how resilient a configuration is to variations in its topology. The methodology is outlined as follows: First, we choose to vary the configuration, and for this paper, we choose the HSX standard case as our base configuration. Next, we determine the "central strike locations," which represent the mean poloidal location or locations of the strike points for each toroidal value. These represent the locations for divertor plates, baffles, and pumps. For the HSX standard case, two poloidal central locations are allowed for each toroidal value, although for the standard configuration, there is a section where there is only one poloidal center. Finally,

FIG. 13. Strike point scatter plot for three configurations with the wall at 2 cm outside LCFS. The configurations are standard (red x), large island (green +), and small island (black dot). Strike regions that do not exist in the standard configuration are circled.
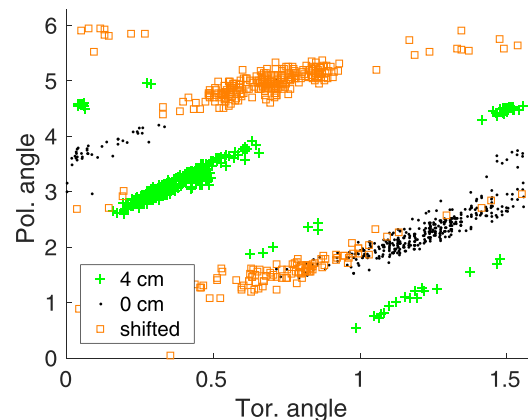

FIG. 15. Strike point scatter plot for large island configuration with magnetic diffusion for wall positions 0 cm outside LCFS (black dots), 4 cm (green +), and a shifted wall (orange circles).
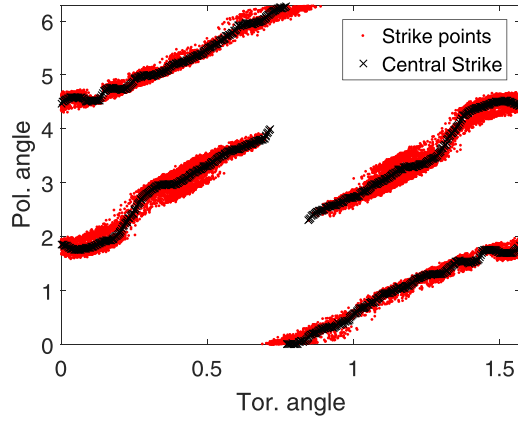
FIG. 16. Average strike point locations for the standard configuration with the wall at 4 cm from LCFS.

we evaluate the degree in which the configurational variations adhere to the same strike pattern.

The calculation of the strike centers for the standard configuration with a 4 cm wall position is shown in Figure 16. The strike points were calculated using the diffusion method with $D = 0.5$ m^2/s. The central strike locations were determined by separating the strike points into toroidal bins and then finding the poloidal mean value for each toroidal group. For most toroidal bins, two groups are present, but for the section between the toroidal angles ∼0.71 and 0.85 radians, corresponding to the "triangle" section of HSX, only one poloidal group is present. Finally, the central strike lines are smoothed to remove noise from the Monte Carlo sampling.

Next, we determine how closely a given strike point pattern adheres to the central strike locations. This is done by determining the poloidal distance for each individual point in the Monte Carlo sample to the nearest central strike location. Then, we calculate the percentage of points that fall outside a given poloidal section. Then, it is possible to compare different variations of the standard configuration by calculating the poloidal distances for each variation to the same central strike locations. The three configurations where the plasma current is varied are shown in Figure 17. All three lines lie nearly on top of each other, indicating that there is essentially no difference in the strike profile of the

configurations. This leads to the conclusion that the HSX standard configuration is resilient to changes in plasma current and pressure.

For the sake of comparison, we also show a variation type where there is no resilience. We choose the HSX standard configuration with a wall at 1 cm from the LCFS and adjust the auxiliary coils to introduce large islands into the edge. The calculation of the strike point distance from the central strike locations for the auxiliary coil calculation is shown in Figure 18. It is clear that the configuration with large islands has numerous strike points that are located a significant distance from the central strike locations. Even for the small island configuration, there are larger deviations as compared to the standard configuration, although the deviation is much smaller and the vast majority of the points lie a small distance from the central strike lines. The conclusion is the same as above, and resilience of HSX can be broken with the introduction of large islands that intersect wall components.

VII. EMC3-EIRENE SIMULATIONS

The strike point calculations are a useful initial step where heat and particle flux are likely to fall. However, the reality of calculating actual heat flux amounts is not possible with these simple methods.

We engage in a deeper examination of the problem by comparing the simple strike point calculation with more detailed EMC3-EIRENE simulations.[36,44] EMC3 is a 3-D fluid Monte-Carlo code, and it is coupled to EIRENE, which is a kinetic neutral solver. The coupled codes solve for the electron and ion temperatures, electron and neutral densities, and ion parallel flows at all points in the plasma edge. In addition, it solves for the heat and particle fluxes on the targets. The input parameters for these simulations are the plasma density at the inner simulation boundary and the power through that boundary. The wall positioning is closest to the 4 cm outside the LCFS (Figure 3). We examine the three configurations corresponding to the small, medium, and large islands discussed in Section V D, for wall positions outside the island chains. These configurations were examined in more detail in Ref. 36; however, here we present the
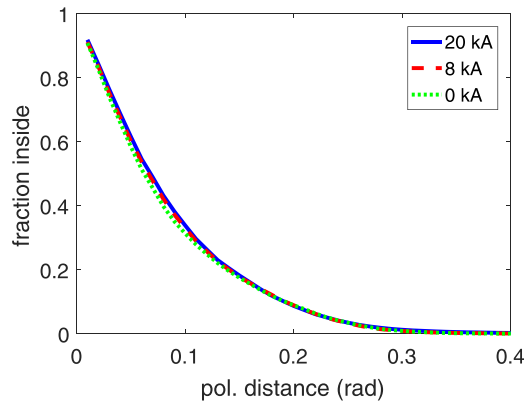

FIG. 17. Evaluation of resilience for three different values of plasma current: 20 kA (blue solid), 8 kA (red dashed), and no current (green dotted).
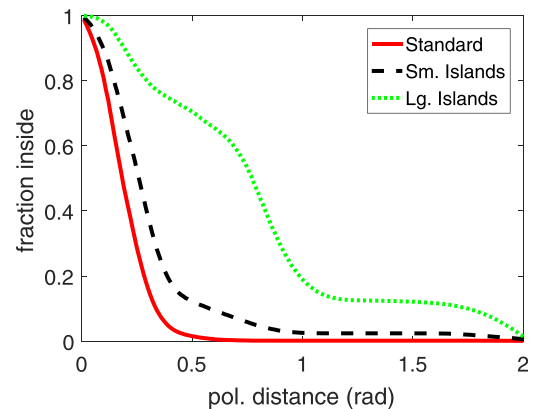

FIG. 18. Evaluation of resilience for three different edge configurations representing standard configuration (red solid), small islands (black dashed), and large islands (green dotted).
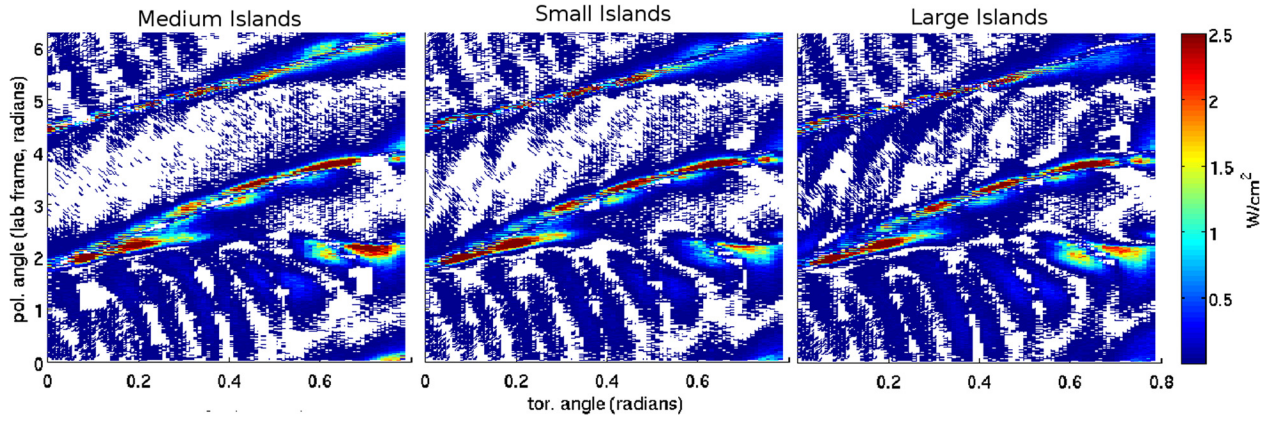
FIG. 19. EMC3-EIRENE calculation of heat flux deposition for medium (left), small (middle), and large (right) island configurations.

measurements of heat fluxes in the low recycling regime, shown in Figure 19.

It is clear from these simulations that the heat flux is relatively uniform between the three configurations. Also, the helical stripes of the heat flux align with the strike point calculations with the magnetic diffusion method.

Unfortunately, it is not yet possible to transition from a VMEC equilibrium with finite current to a full EMC3 simulation, so we are limited to examining the vacuum cases. Nevertheless, the agreement between the simple strike point model and the full EMC3-EIRENE plasma simulations indicates that the equilibria with plasma currents should extrapolate similarly.

VIII. DISCUSSION

We pose the following question: do the locations of the strike lines correlate with any easily understandable geometrical property of either the vessel or the field lines? The answer is yes. Figure 20 shows the strike lines for the standard configuration overlaid on a contour plot of the first principal curvature of the vessel. Because the vessel shape is conformal to the last closed flux surface shape, the result is equivalent to the curvature of the LCFS. It is clear that strike points lie along regions of the peak curvature, although they
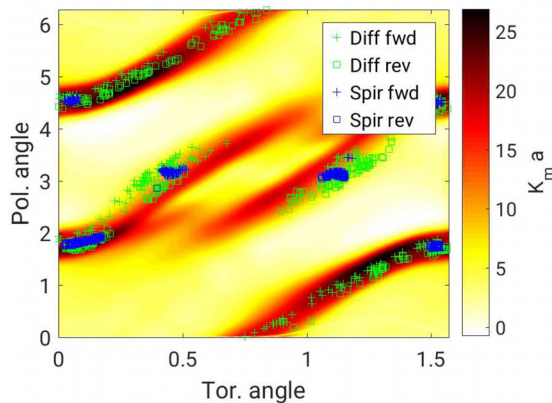

FIG. 20. Strike points for magnetic diffusion and spiral method overlaid onto a plot of the curvature of the LCFS. Curvature values are normalized to the machine major radius.

are not exactly correlated with the toroidal peaks of the curvature.

The connection between the curvature of the LCFS and divertor resilience was discussed by Boozer in Ref. 25. Boozer describes "sharp edges" as a necessary feature of resilient divertors and that these should be a natural feature of most optimized stellarator equilibria. The hypothesis is that plasma flux is likely to preferentially leave through the LCFS from regions of high curvature. Because the location of the LCFS is not known, it is not easy to determine whether this hypothesis is true. Nevertheless, the hypothesis is supported from measurements presented in Section V B. There it was found that when moving the wall position inwards, the location of the strike points remain constant and at regions of high curvature.

Comparing Figure 20 with Figure 2 is useful, which showed the curvature of the last closed flux surface and the field lines that lay along the high curvature regions. Unsurprisingly, the high curvature regions at the wall are in the same locations as the high curvature regions of the LCFS. This is because the wall and the LCFS are of the same shape. However, the wall curvature regions are significantly less sharp than on the LCFS. Nevertheless, the strike lines still tend to favor the regions of the highest curvature.

An interesting point is that one of the defining features of the equilibria with plasma current is a change in the magnitude of the plasma curvature on the LCFS. However, this alteration in the LCFS curvature did not degrade the locations of the strike points. A possible explanation is that there are some critical curvature values that provide strike point stability. Another possibility is that as long as the region of maximum curvature exists, it does not matter how much larger it is than other nearby regions. Nevertheless, more work needs to be done in defining what link exists between the curvature of the LCFS and the behavior of the divertor.

Another correlation can be seen in Figure 21 where the strike lines are plotted over a contour plot of $\mathbf{B} \cdot \mathbf{n}$ at the vessel wall. The strike lines lie on helical seams, where $\mathbf{B} \cdot \mathbf{n}$ is close to zero and is between the regions of the strong normal field in opposite directions. Therefore, unsurprisingly, the strike lines appear on field lines that have the maximal radial excursion. The system can also be thought of in a Hamiltonian sense. The points where the field lines cross any
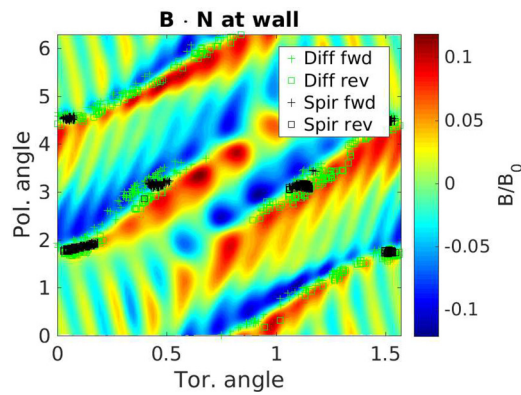
FIG. 21. Strike points for magnetic diffusion and spiral method overlaid onto a plot of **B** · **n** at the target normalized to the magnetic field at the magnetic axis.

near tangential surface outside the LCFS can be thought of as Hamiltonian turnstiles.[25,45] The results presented earlier in this paper indicate that the areas of maximal radial excursion are a property of the gross geometry. For conformal vessels, in which the position of the targets is a uniform distance from the LCFS, the strike lines will always lie in specific regions.

IX. CONCLUSION

Quasi-helically symmetric configurations, as embodied by the HSX design, demonstrate resilient divertor properties. The edge of HSX demonstrates resiliency to specific configuration changes in that the strike point locations do not move significantly. Most importantly, the strike point profile remains consistent with variations in internal plasma current. However, in configurations with large edge islands that intersect wall components, resiliency is not maintained. In large-island configurations, strike point patterns can vary significantly.

The resiliency of the strike point position is necessary but does not guarantee fulfillment of all the desired properties of an advanced divertor, namely, that the full edge behavior including recycling properties, neutral pumping, impurity penetration, particle flux, and heat flux is within required limits and remains constant with configuration and profile changes. On the broad topic of advanced divertor behavior, the edge physics models are still under development and require validation from the experiment. There is a considerable need for high performance quasi-symmetric stellarators that can test divertor resiliency directly.

ACKNOWLEDGMENTS

[1] N. Ohyabu and H. Renner, Contrib. Plasma Phys. **38**, 94–105 (1998).
[2] R. König, P. Grigull, K. McCormick, Y. Feng, J. Kisslinger, A. Komori, S. Masuzaki, K. Matsuoka, T. Obiki, N. Ohyabu, H. Renner, F. Sardei, F. Wagner, and A. Werner, Plasma Phys. Controlled Fusion **44**, 2365–2422 (2002).
[3] T. K. Mau, T. B. Kaiser, A. A. Grossman, A. R. Raffray, X. R. Wang, J. F. Lyon, R. Maingi, L. P. Ku, M. C. Zarnstorff, and ARIES-CS Team, Fusion Sci. Technol. **54**, 771 (2008).
[4] H. Renner, J. Boscary, V. Erckmann, H. Greuner, H. Grote, J. Sapper, E. Speth, F. Wesner, M. Wanner, and W7-X Team, Nucl. Fusion **40**, 1083 (2000).
[5] M. Kobayashi, Y. Feng, Y. Xu, F. L. Tabares, K. Ida, O. Schmitz, T. E. Evans, H. Frerichs, Y. Liang, A. Bader, K. Itoh, H. Yamada, Ph. Ghendrih, G. Ciraolo, D. Tafalla, A. Lopez-Fraguas, H. Y. Guo, Z. Y. Cui, D. Reiter, N. Asakura, U. Wenzel, S. Morita, N. Ohno, B. J. Peterson, and S. Masuzaki, J. Nucl. Mater. **463**, 2–10 (2015).
[6] H. Renner, J. Boscary, H. Greuner, H. Grote, F. W. Hoffmann, J. Kisslinger, E. Strumberger, and B. Mendelevitch, Plasma Phys. Controlled Fusion **44**, 1005 (2002).
[7] H. Greuner, B. Bswirth, J. Boscary, T. Friedrich, C. Lavergne, Ch. Linsmeier, J. Schlosser, and A. Wiltner, Fusion Eng. Des. **84**, 848–852 (2009).
[8] Y. Kubota, N. Noda, A. Sagara, R. Sakamoto, O. Motojima, I. Fujita, T. Hino, T. Yamashina, K. Tokunaga, and N. Yoshida, Fusion Eng. Des. **39–40**, 247–252 (1998).
[9] J. D. Lore, T. Andreeva, J. Boscary, S. Bozhenkov, J. Geiger, J. H. Harris, H. Hoelbe, A. Lumsdaine, D. McGinnis, A. Peacock, and J. Tipton, IEEE Trans. Plasma Sci. **42**, 539 (2014).
[10] T. Morisaki, S. Masuzaki, M. Kobayashi, M. Shoji, J. Miyazawa, R. Sakamoto, G. Motojima, M. Goto, H. Funaba, H. Tanaka, K. Tanaka, I. Yamada, S. Ohdachi, H. Yamada, A. Komori, and the LHD Experiment Group, Nucl. Fusion **53**, 063014 (2013).
[11] S. Masuzaki, M. Kobayashi, M. Shoji, M. Tokitani, T. Morisaki, R. Sakamoto, M. Osakabe, T. Murase, T. Kobuchi, H. Yonezu, Y. Takeiri, H. Yamada, A. Komori, and the LHD Experiment Group, Plasma Fusion Res. **6**, 1202007 (2011).
[12] K. McCormick, P. Grigull, R. Burhenn, H. Ehmler, Y. Feng, L. Giannone, G. Haas, and F. Sardei, J. Nucl. Mater. **337–339**, 520–524 (2005).
[13] H. Grote, J. Kisslinger, H. Renner, J. Boscary, H. Greuner, F. W. Hoffmann, and B. Mendelevitch, J. Nucl. Mater. **313–316**, 1298–1303 (2003).
[14] R. Burhenn, Y. Feng, K. Ida, H. Maassberg, K. J. McCarthy, D. Kalinina, M. Kobayashi, S. Morita, Y. Nakamura, H. Nozato, S. Okamura, S. Sudo, C. Suzuki, N. Tamura, A. Weller, M. Yoshinuma, and B. Zurro, Nucl. Fusion **49**, 065005 (2009).
[15] S. Dai, M. Kobayashi, G. Kawamura, S. Morita, T. Oishi, H. M. Zhang, X. L. Huang, Y. Feng, D. Z. Wang, Y. Suzuki, and the LHD Experiment Group, Contrib. Plasma Phys. **56**, 628–633 (2016).
[16] O. Schmitz, K. Ida, M. Kobayashi, A. Bader, S. Brezinsek, T. E. Evans, H. Funaba, M. Goto, O. Mitarai, T. Morisaki, G. Motojima, Y. Nakamura, Y. Narushima, D. Nicolai, U. Samm, H. Tanaka, H. Yamada, M. Yoshinuma, Y. Xu, the TEXTOR, and LHD Experiment Groups, Nucl. Fusion **56**, 106011 (2016).
[17] A. Bader, M. Kobayashi, O. Schmitz, A. R. Akerson, F. Effenberg, H. Frefichs, Y. Feng, C. C. Hegna, K. Ida, and the LHD Experimental Group, Plasma Phys. Controlled Fusion **58**(12), 124006 (2016).
[18] C. R. Burnett, D. J. Grove, R. W. Palladino, T. H. Stix, and K. E. Wakefield, Phys. Fluids **1**, 438 (1958).
[19] J. Nuhrenberg and R. Zille, Phys. Lett. A **129**, 113 (1988).
[20] J. M. Canik, D. T. Anderson, F. S. B. Anderson, K. M. Likin, J. N. Talmadge, and K. Zhai, Phys. Rev. Lett. **98**, 085002 (2007).
[21] M. C. Zarnstorff, L. A. Berry, A. Brooks, E. Fredrickson, G. Y. Fu, S. Hirshman, S. Hudson, L. P. Ku, E. Lazarus, and D. Mikkelsen, Plasma Phys. Controlled Fusion **43**, A237 (2001).
[22] N. Ohyabu, T. Watanabe, H. Ji, H. Akao, T. Ono, T. Kawamura, K. Yamazaki, K. Akaishi, N. Inoue, A. Komori, Y. Kubota, N. Noda, A. Sagara, H. Suzuki, O. Motojima, M. Fujiwara, and A. Iiyoshi, Nucl. Fusion **34**, 387 (1994).
[23] Y. Feng, F. Sardei, P. Grigull, K. McCormick, J. Kisslinger, and D. Reiter, Nucl. Fusion **46**, 807 (2006).
[24] E. Strumberger, Nucl. Fusion **36**, 891 (1996).
[25] A. H. Boozer, J. Plasma Phys. **81**, 515810606 (2015).
[26] F. S. B. Anderson, A. F. Almagri, D. T. Anderson, P. G. Matthews, J. N. Talmadge, and J. L. Shohet, Fusion Technol. **27**, 273 (1995).
[27] Y. Feng, M. Kobayashi, T. Lunt, and D. Reiter, Plasma Phys. Controlled Fusion **53**, 024009 (2011).
[28] G. Grieger, W. Lotz, P. Merkel, J. Nuhrenberg, J. Sapper, E. Strumberger, H. Wobig, R. Burhenn, V. Erckmann, U. Gasparino, L. Giannone, H. J. Hartfuss, R. Jaenicke, G. Kuhner, H. Ringler, A. Weller, F. Wagner, the W7-X Team, and the W7-AS Team, Phys. Fluids B **4**, 2081 (1992).
[29] T. Morisaki, K. Narihara, S. Masuzaki, S. Morita, M. Goto, A. Komori, N. Ohyabu, O. Motojima, K. Matsuoka, and the LHD Experimental Group, J. Nucl. Mater. **313–316**, 548–552 (2003).

[30]P. Grigull, K. McCormick, H. Renner, S. Masuzaki, R. Knig, J. Baldzuhn, S. Bumel, R. Burhenn, R. Brakel, H. Ehmler, Y. Feng, F. Gadelmeier, L. Giannone, D. Hartmann, D. Hildebrandt, M. Hirsch, R. Jaenicke, J. Kisslinger, T. Klinger, J. Knauer, D. Naujoks, H. Niedermeyer, E. Pasch, N. Ramasubramanian, F. Sardei, F. Wagner, U. Wenzel, and A. Werner, Fusion Eng. Des. **66–68**, 49–58 (2003).

[31]J. C. Schmitt, J. N. Talmadge, and D. T. Anderson, Nucl. Fusion **53**, 082001 (2013).

[32]D. Sharma, Y. Feng, and F. Sardei, Nucl. Fusion **46**, S127 (2006).

[33]Y. Feng, M. Kobayashi, T. Morisaki, S. Masuzaki, J. Miyazawa, B. J. Peterson, S. Morita, M. Shoji, K. Ida, I. Yamada, K. Narihara, N. Ashikawa, H. Yamada, N. Ohyabu, A. Komori, O. Motojima, F. Sardei, D. Reiter, and the LHD Experimental Group, Nucl. Fusion **48**, 024012 (2008).

[34]G. Park, C. S. Chang, I. Joseph, and R. A. Moyer, Phys. Plasma **17**, 102503 (2010).

[35]A. R. Akerson, A. Bader, C. C. Hegna, O. Schmitz, L. A. Stephey, D. T. Anderson, F. S. B. Anderson, and K. M. Likin, Plasma Phys. Controlled Fusion **58**, 084002 (2016).

[36]A. Bader, D. T. Anderson, C. C. Hegna, Y. Feng, J. D. Lore, and J. N. Talmadge, Nucl. Fusion **53**, 113036 (2013).

[37]E. Strumberger, Nucl. Fusion **32**, 737 (1992).

[38]A. Punjabi and A. H. Boozer, Phys. Lett. A **378**, 2410 (2014).

[39]S. Lazerson, M. Otte, S. Bozhenkov, C. Biedermann, T. S. Pedersen, and the W7-X Team, Nucl. Fusion **56**, 106005 (2016).

[40]S. P. Hirshman and W. I. van Rij, Comput. Phys. Commun. **39**, 161 (1986).

[41]A. D. Turnbull, W. A. Cooper, L. L. Lao, and L. P. Ku, Nucl. Fusion **51**, 123011 (2011).

[42]H. Hölbe, T. S. Pedersen, J. Geiger, S. Bozhenkov, R. Koenig, Y. Feng, J. Lore, A. Lumsdaine, and the W7-X Team. Nucl. Fusion **56**, 026015 (2016).

[43]S. P. Gerhardt, J. N. Talmadge, J. M. Canik, and D. T. Anderson, Phys. Rev. Lett. **94**, 015002 (2005).

[44]Y. Feng, F. Sardei, J. Kisslinger, P. Grigull, K. McCormick, and D. Reiter, Contrib. Plasma Phys. **44**, 57–69 (2004).

[45]J. D. Meiss, Chaos **25**, 097602 (2015).